Supplementary Information

Coherent satellites in multi-spectral regenerative frequency microcombs

Supplementary Note 1: Numerically modeled symmetric satellite comb coherence

The comb spectrum is numerically modeled using Lugiato-Lefever equation (LLE) [1,2],

$$t_R \frac{\partial E(t,\tau)}{\partial t} = \left[-\alpha - i\delta_0 + iL\sum_{k\geq 2}\frac{\beta_k}{k!}\left(i\frac{\partial}{\partial \tau}\right)^k + i\gamma L|E|^2\right]E + \sqrt{\theta}E_{in}$$

where t_R is the round-trip time, α is the total cavity loss, θ is the power transmission coefficient, δ_0 is the phase detuning between the pump frequency and the pumped cavity resonance, β_k is the Taylor series expansion coefficient of the propagation constant and γ is the nonlinear coefficient. In the model, simulated dispersion up to the fourth-order dispersion (FOD) is included.

Supplementary Figure 1 shows two examples of simulation result of the symmetric satellite comb in comparison with experimental observation in Figure 1a (Supplementary Figure 1a) and 1d (Supplementary Figure 1b). The left panels show the full evolution in the spectral domain, where the symmetric satellite combs are marked in dashed boxes, whereas the right panels plot the spectra and temporal shapes at different detunings. In both examples, the comb starts with a Turing pattern extended beyond modulation instability bandwidth (temporal quasi-sinusoidal shape) as shown in panel (I), then gradually experiences sub-comb commensuration [from panel (II) to (III)]. The satellite centroids shift by one mode from stage (II) to stage (III) due to increased intra-cavity power, qualitatively agreeing with experimental observations. A comparison of temporal shape is shown in panel (IV) for stage (II) and (III). Stage (II) shows nearly quasi-sinusoidal shape while stage (III) experiences only an additional side peak in each period, indicating the mutual coherence between the central comb and the symmetric satellite.

From (II) to a(III) in Supplementary Figure 1a, the satellite centroid shifts from 290th to 291st of azimuthal mode number, in well agreement with experimental observations qualitatively. In Supplementary Figure 1b, the satellite centroid shifts from 204rd to 205th of azimuthal mode number, agreeing with experiments qualitatively too.

Indicated in stages (II) of Supplementary Figure 1a and 1b, both satellite and central combs generate their own sidebands. Competing effects occur between satellite and central combs as detuning grows. As detuning increases from blue to red, the symmetric combs disappear and reappear.

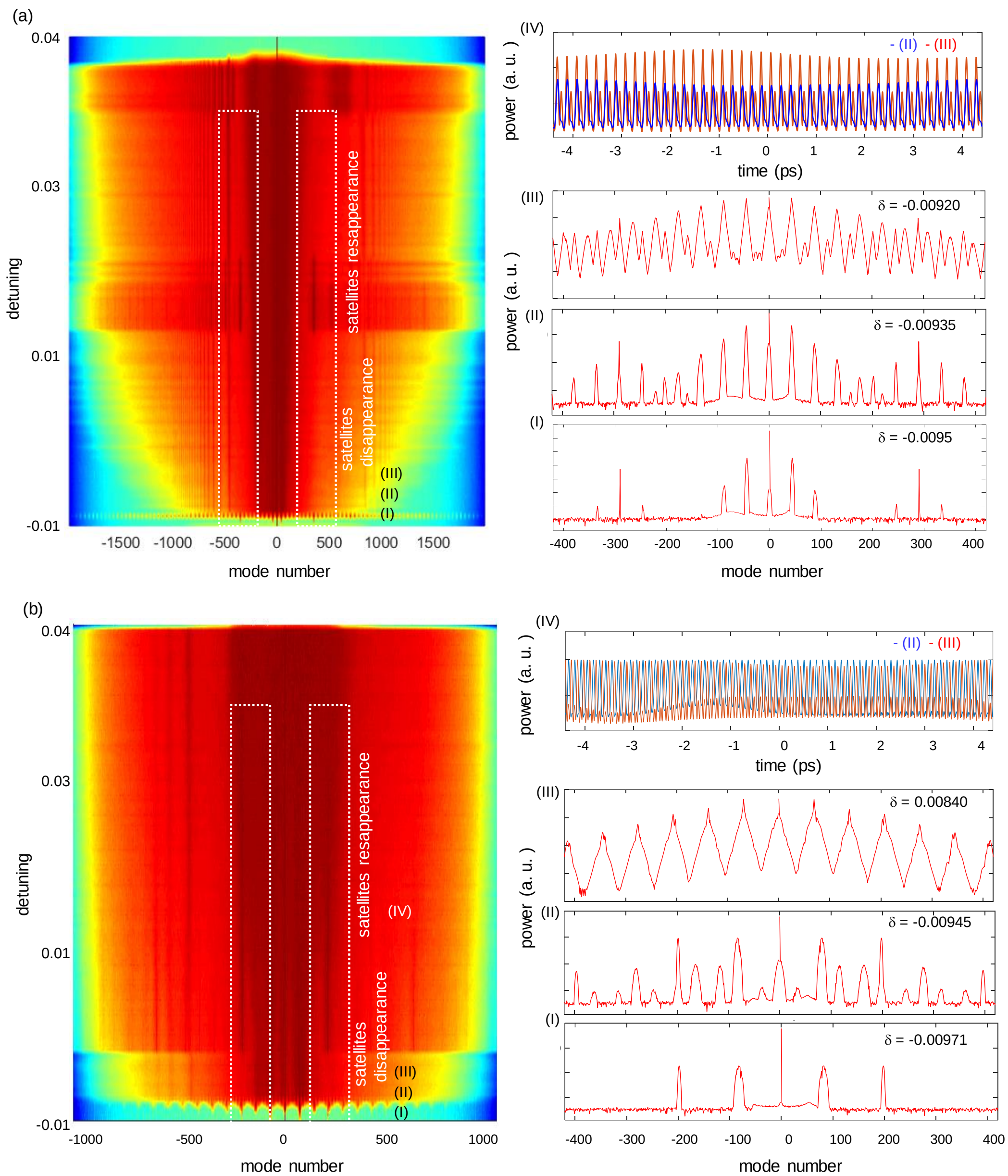

Supplementary Figure 1. Numerically modeled frequency comb spectra corresponding to: (**a**) Figure 1a of the main text, and (**b**) Figure 1d of the main text. Simulation parameters: (**a**) on-chip power of 0.3W, GVD = -30 fs^2/mm, TOD = -1,000 fs^3/mm, TOD = 8,000 fs^4/mm; (**b**) on-chip power of 0.25W, GVD = -10 fs^2/mm, TOD = -658 fs^3/mm, TOD = 5,000 fs^4/mm. Each example shows the spectra at three detuning stages [panel (I) to (III)], and a comparison of temporal shape at two detunings [panel (IV)].

Illustration of satellite comb formation with multiple parametric gain regimes: We provide an illustrate schematic that shows the multiple parametric gain regimes with respect to cavity resonances on the frequency scale as shown in Supplementary Figure 2. Given the limited bandwidth of MI when $\beta_2 < 0$, the phase matching can still reappear when the azimuthal mode number is larger owing to the higher-order dispersion that can inversely balance the phase mismatch, i.e. a large positive β_4. Different from the case in the prior work [3], where the mismatch can reach to the FSR of the *m*th mode, here the symmetric satellite get phase matched with azimuthal mode number of signal and idler resonances equals. The momentum conservation is naturally satisfied even in a uniform waveguide.

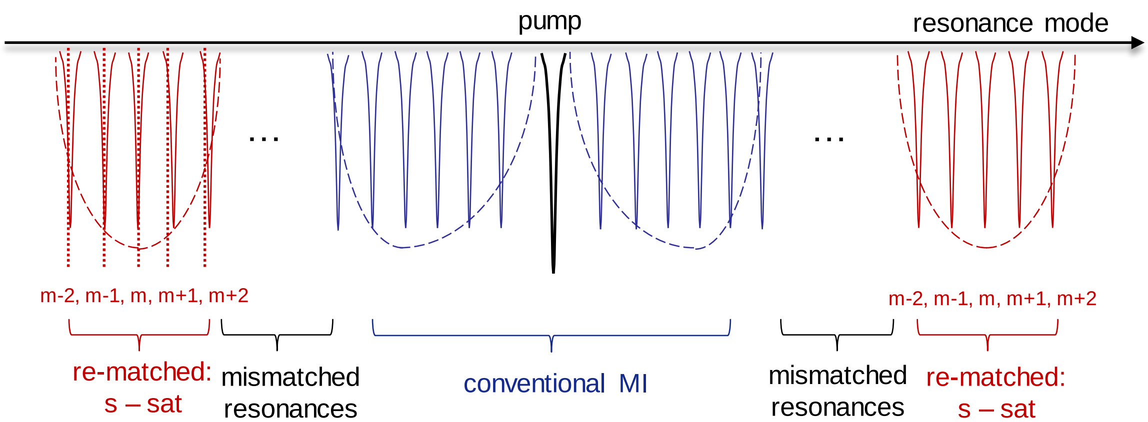

Supplementary Figure 2. Illustration of satellite comb formation with multiple parametric gain regimes: conventional modulation instability (MI, blue), mismatched modes (black), and re-matched modes that generate symmetric satellite comb (s – sat, red). Gain bandwidth exist (dashed blue and red curved envelope) due to the local dispersion balancing the nonlinearity, resulting the mismatched modes in between. Round dot lines show the resonance frequencies that are mirror of the signal modes with respect to the pump.

Supplementary Note 2: Phase-matching calculation and its dependence on higher-order dispersion (HOD)

Following the discussion in the main text on the microring with cross-section of 1600 × 800 nm^2, phase mismatch is calculated at each cavity mode with respect to the pump mode, where the simulated group velocity through finite element method [4] is used to simulate the cavity free-spectral-range (FSR). We note that higher-order dispersion plays an important role in determining the phase-matching wavelength of satellite combs. An example is shown Supplementary Figure 3, pumped at 1585 nm with 30.5 dBm coupled power, comparing the phase-matching considering all orders of dispersion and dispersion only up to fourth-order, i.e. GVD, TOD and FOD. The calculated phase matched modes for symmetric satellites are closer to experimental observations if neglecting HOD above fourth order. This suggests that the uncertainty of HOD, which is hard to determine experimentally, contributes to the discrepancy of phase-matching prediction, similar to the previous conclusion [3]. Only even-order dispersion affect the phase-matching condition of

FWM [5,6]; uncertainty on the exact higher-order (4th, 6th or even 8th) will influence the theoretical predictions. When GVD is relatively small, FOD can dominate the phase-matching.

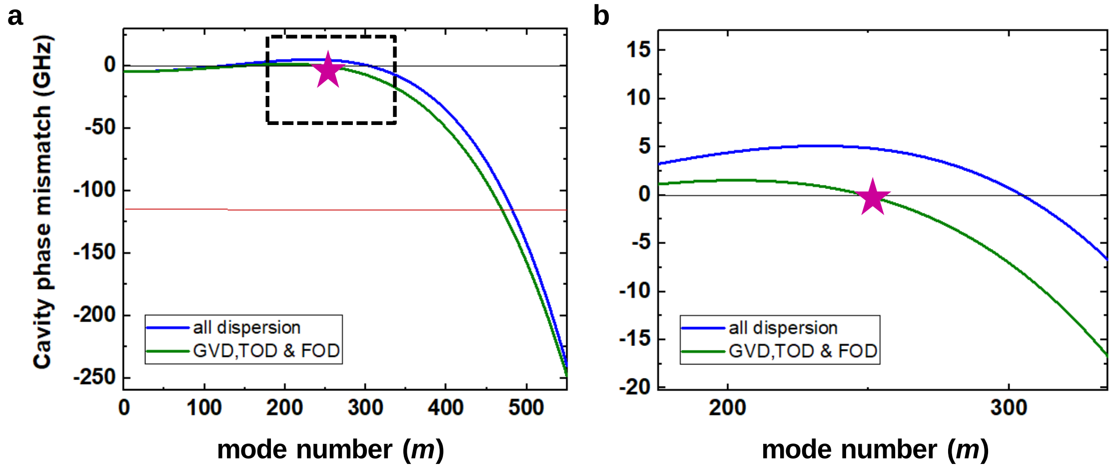

Supplementary Figure 3. Influence of higher-order dispersion (HOD) on satellite phase-matching. a, Cavity phase-matching of satellites considering all orders of dispersion (blue) and dispersion only up to fourth order, i.e. GVD, TOD and FOD (green), in comparison with experimental data (magenta stars). **b,** Zoom-in views for symmetric satellite. The phase-matching calculation is closer to experimental observation neglecting HOD above 4^{th} order, suggesting the uncertainty of HOD contributes to the discrepancy of phase-matching prediction.

Supplementary Note 3: High-efficiency *f-2f* stabilization approach based on octave spanning satellite frequency combs

Here we show the comparison of theoretical analysis and experimental observations of satellite maps in another microcavity with a different geometry, i.e. with cross-section of 1500 × 800 nm^2. Compared to the device discussed mostly in main text, this one features with slightly smaller anomalous GVD and more negative TOD (Supplementary Figure 4). From the theory developed in main text, the tunability of satellite mode per pump mode is higher given the same spectral shift, leading to a broader overall spanning of the satellites. Experimental results show close to an octave spanning from this device (Figure 1g in main text).

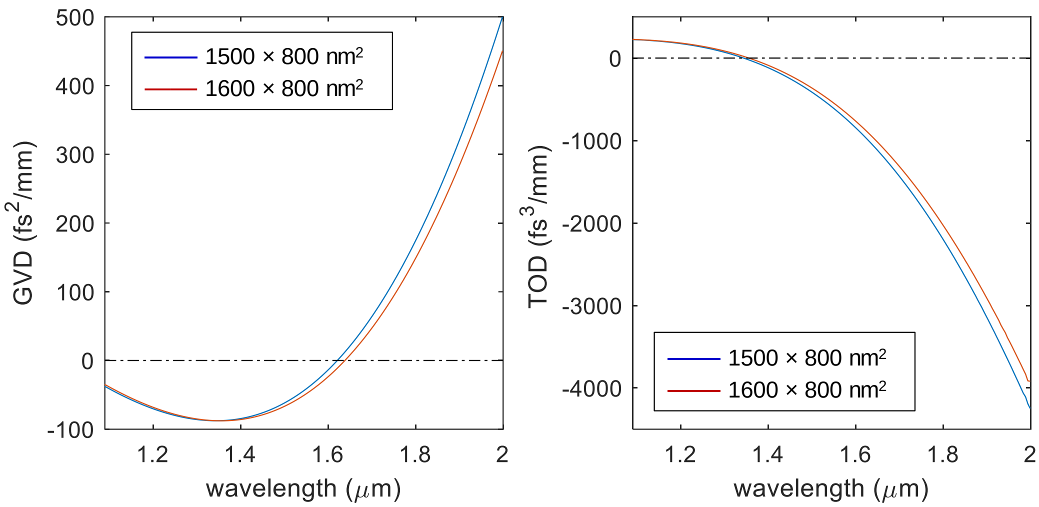

Supplementary Figure 4. Simulated dispersion of microcavity with slightly different waveguide cross-sections of 1500 × 800 nm^2 (blue) and 1600 × 800 nm^2 (red). a, Group velocity dispersion (GVD). **b,** Third-order dispersion (TOD). Both devices show high TOD, with the 1500 × 800 nm^2 (blue) having an even higher value of TOD and higher ratio between TOD and GVD, supporting a broader spectrum of satellite comb.

Pumping at different resonances with varied coupled powers, we map the spectral centroids of symmetric satellites and dispersive waves in Supplementary Figure 5, similar to that shown in Figure 4a.

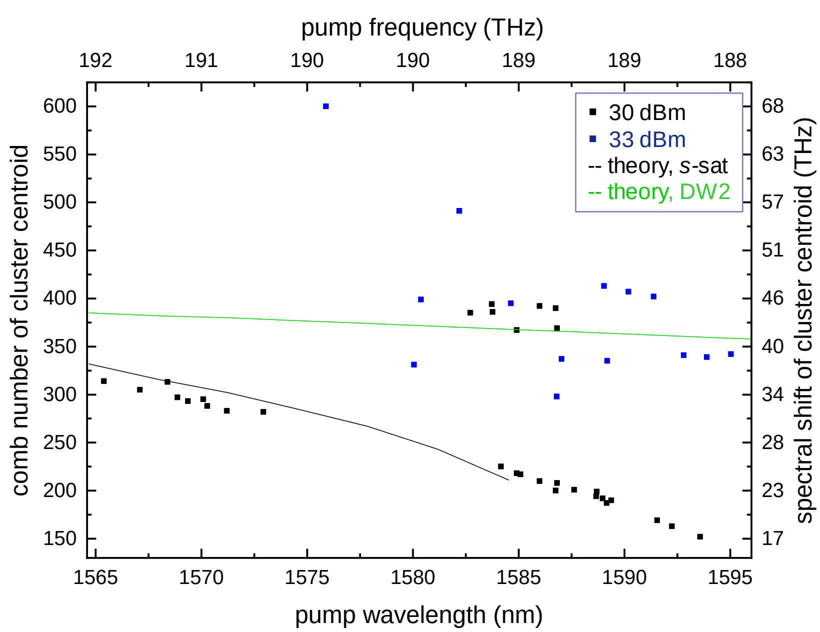

Supplementary Figure 5. Observed summary satellite map versus theoretical comparison in another microcavity with cross-section of 1500 × 800 nm^2. Plotted simulated curves are modeling for symmetric satellites (black) and dispersive wave (green).

Particularly when pumped at 1578.92 nm and 1581.60 nm, the centroids of the short-wavelength dispersive waves locate at 1159.80 nm and 1184.28 nm respectively as shown in Supplementary Figure 6. The total span of the DW centroids can potentially span up to an octave.

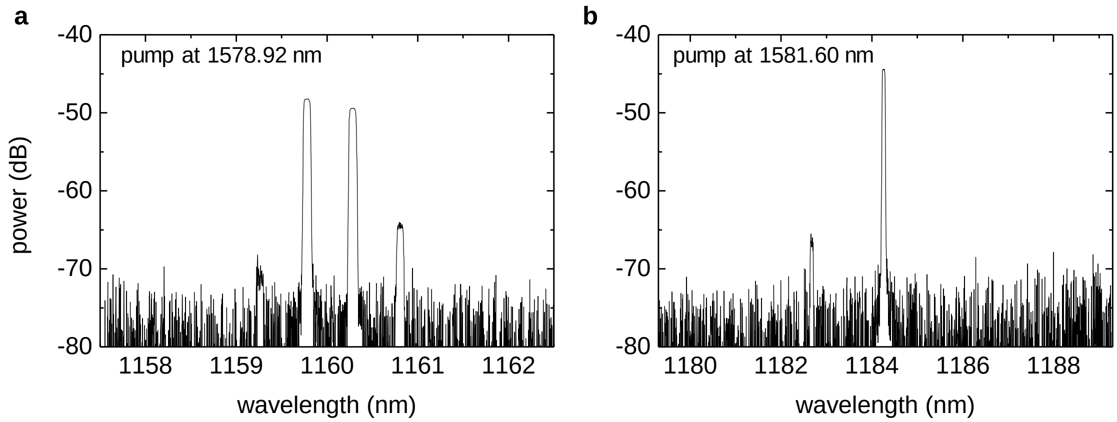

Supplementary Figure S6. Short-wavelength dispersive waves. When pumping at 1578.92 nm and 1581.60 nm, the centroids of the short-wavelength dispersive waves are located at 1159.80 nm and 1184.28 nm respectively. Long-wavelength dispersive waves lie beyond the detection range of our optical spectrum analyzers (OSAs), leading to expected spanning of more than one octave of the dispersive wave centroids.

Supplementary Note 4: Other frequency combs with satellites pumped at C-band

With the same cavity with waveguide cross-section of 1600×800 nm^2, at pumping wavelength where the ratio of second- and third-order dispersion is larger than that in Figure 3a and 3b, the dispersive wave (Čerenkov radiation) peak can also be in the central comb as shown in Supplementary Figure 7.

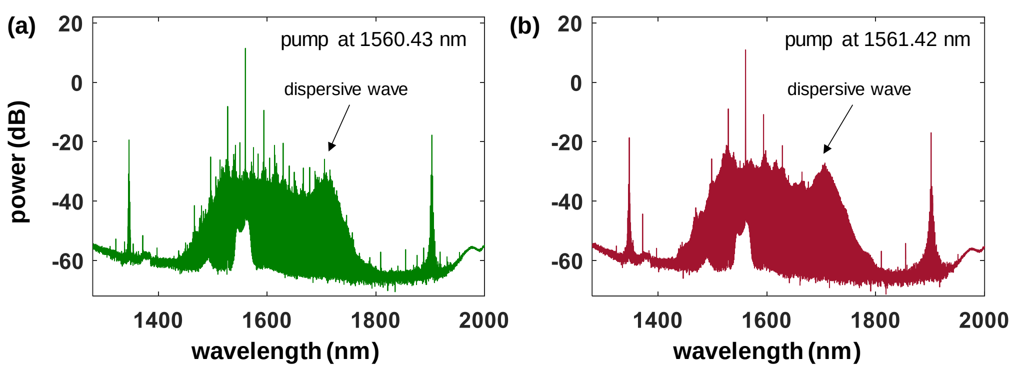

Supplementary Figure 7. Satellite combs pumping at 1560.43 nm and 1561.40 nm respectively. As the ratio of third- and second-order dispersion, i.e. $\frac{|\beta_2|}{|\beta_3|}$, becomes larger, the dispersive wave (Čerenkov radiation) can also be observed within the central comb.

Supplementary Note 5: Evolution dynamics of symmetric idler satellites and short-wavelength dispersive wave

Supporting the symmetric signal satellite frequency combs detailed in main text, the idler satellites also evolve with similar dynamical transition and radio-frequency (RF) amplitude noise, as shown in Supplementary Figure 8.

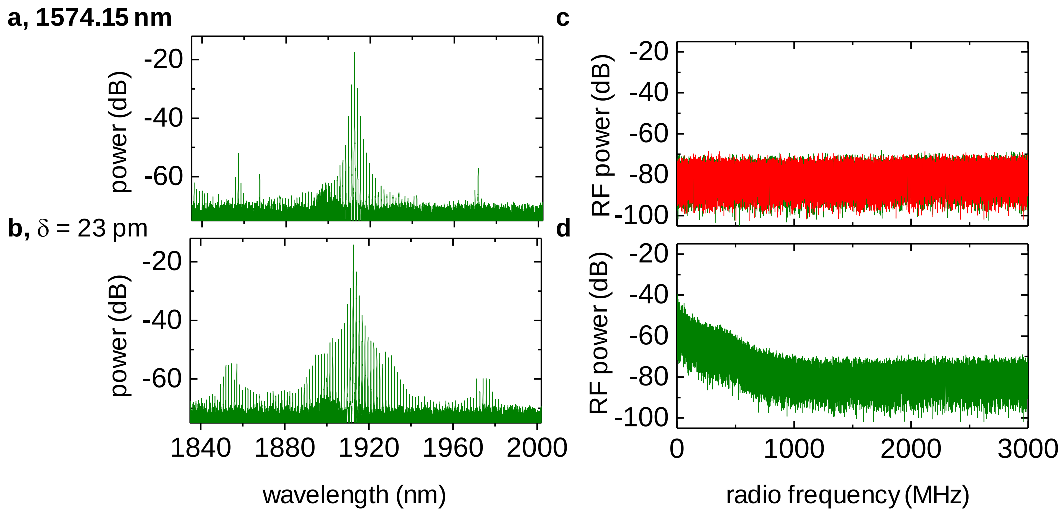

Supplementary Figure 8. Coherence evolution of the symmetric idler satellite combs. a and **b,** series of satellite comb spectra with step-wise detuning of the pump frequency from blue to red over 23 pm. **c** and **d,** corresponding RF amplitude noise measurement. Red curve in **c** plots the detector background noise, indicating the low phase noise operation and coherent state of **a**.

The short-wavelength dispersive wave shows similar dynamical evolution with that of the symmetric satellite, shown in Supplementary Figure 9. Two-FSRs spaced coherent comb is generated firstly (Supplementary Figure 9a); with pump laser further detuned into resonance, a broader single-FSR satellite comb is obtained (Supplementary Figure 9b), where high frequency noise occurs. Again, with laser-cavity detuning control, the comb can be driven to self-injection locked states with low noise [7,8] (Supplementary Figure 9c).

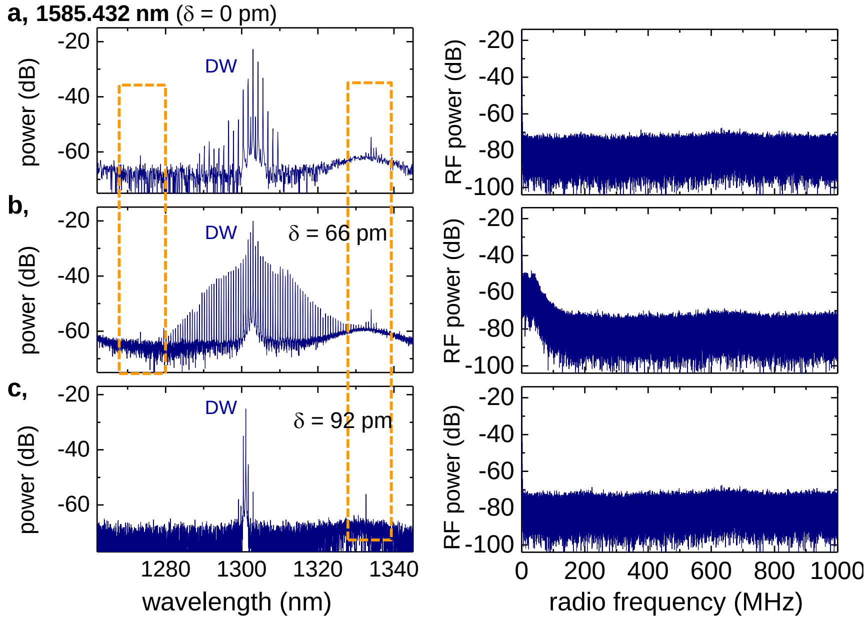

Supplementary Figure 9. Coherence evolution of the short-wavelength dispersive wave. Example evolution are shown through the optical spectrum and RF amplitude noise. Once generated, the dispersive wave evolves in a similar manner as the symmetric satellites. Within orange boxes are the secondary satellite sidebands from local MI directly from dispersive wave centroids.

Supplementary Note 6: Optical system for microcomb coherence measurement

Given that the comb spacing here is more than our electronic detection bandwidth limit, we introduce the approach of using a wavelength meter to derive the comb spacing with a certain precision as shown in Supplementary Figure 10. A wavelength meter is employed to measure the wavelength of the selected comb mode, with each comb mode individually filtered out by tunable bandpass filters. The repetition rate measured by the i^{th} comb mode is given by the frequency difference between comb frequency and pump frequency divided by mode number. Due to frequency division, the method permits a better precision on measured comb spacing than that of the wavelength meter itself.

The pump laser is phase-locked to a Menlo fiber frequency comb, referenced to ultrastable FP cavity (Stable Laser Systems), with instantaneous linewidth close to 1 Hz to reduce pump frequency drift and resulting comb spacing fluctuation. Major imprecision of the measurement comes from variations of cavity FSR and the pump-cavity detuning. With the chip temperature passively stabilized, the variation of cavity FSR is expected to be dominated by ambient noise, which can be in the hour time-scale. This measurement approach is bounded only by the precision of the wavelength meter. To reduce the measurement imprecision, we limit the measurement duration to a few minutes. Due to the limited extinction ratio of the available O-band filter, we can only measure two modes with the highest intensities in the satellite cluster, i.e. one comb spacing data here.

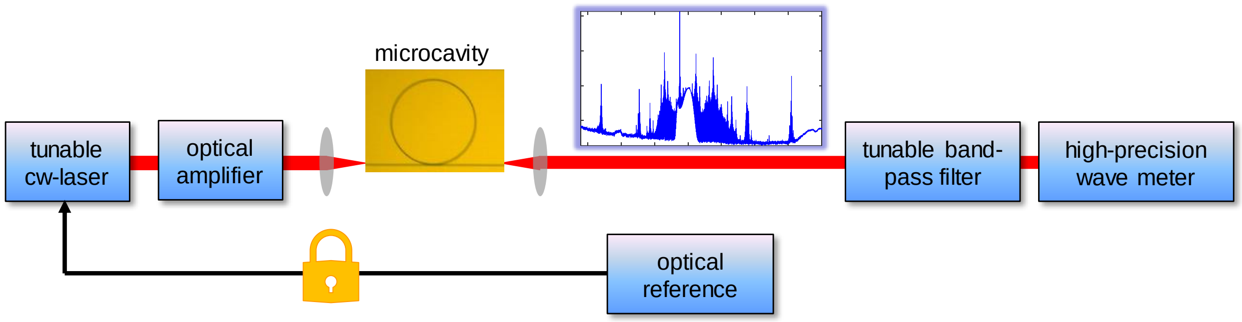

Supplementary Figure 10. Schematic diagram of optical system for microcomb coherence measurement. After locking the pump frequency to an optical reference, the frequencies of central comb and satellites are filtered and measured by a wavelength meter individually. The method permits a better precision on measured comb spacing than that of the wavelength meter itself, due to the frequency division. The total measurement time is controlled within a few minutes, to reduce long-term drift of comb spacing.

Supplementary References

1. S. Coen, H. G. Randle, T. Sylvestre, and M. Erkintalo, "Modeling of octave-spanning Kerr frequency combs using a generalized mean-field Lugiato–Lefever model," Opt. Lett. **38**, 37–39 (2013).
2. C. Bao, Y. Xuan, C. Wang, A. Fülöp, D. E. Leaird, V. Torres-Company, M. Qi, and A. M. Weiner, "Observation of Breathing Dark Pulses in Normal Dispersion Optical Microresonators," Phys. Rev. Lett. **121**, 257401 (2018).
3. S.-W. Huang, A. K. Vinod, J. Yang, M. Yu, D.-L. Kwong, and C. W. Wong, "Quasi-phase-matched multispectral Kerr frequency comb," Opt. Lett., OL **42**, 2110–2113 (2017).
4. S.-W. Huang, J. Yang, M. Yu, B. H. McGuyer, D.-L. Kwong, T. Zelevinsky, and C. W. Wong, "A broadband chip-scale optical frequency synthesizer at 2.7 × 10−16 relative uncertainty," Science Advances **2**, e1501489 (2016).
5. G. P. Agrawal, *Nonlinear Fiber Optics* (Academic Press, 2013).
6. W. H. Reeves, D. V. Skryabin, F. Biancalana, J. C. Knight, P. St. J. Russell, F. G. Omenetto, A. Efimov, and A. J. Taylor, "Transformation and control of ultra-short pulses in dispersion-engineered photonic crystal fibres," Nature **424**, 511–515 (2003).
7. P. Del'Haye, K. Beha, S. B. Papp, and S. A. Diddams, "Self-Injection Locking and Phase-Locked States in Microresonator-Based Optical Frequency Combs," Phys. Rev. Lett. **112**, 043905 (2014).
8. J. Yang, S.-W. Huang, B. H. McGuyer, M. Yu, M. P. McDonald, G. Lo, D.-L. Kwong, T. Zelevinsky, and C. W. Wong, "Bichromatically-pumped coherent Kerr frequency comb with controllable repetition rates," in *Conference on Lasers and Electro-Optics (2016), Paper FM1A.8* (Optical Society of America, 2016), p. FM1A.8.